Phase transition lowering in shock compressed single-crystal aluminum: Atomistic insights

K. Basavaraj ● * and Aditi Ray ●

Theoretical Physics Section, Bhabha Atomic Research Centre, Mumbai 400085, India
and Homi Bhabha National Institute, Mumbai 400094, India

Investigating the shock-induced structural phase transition (PT) in Al is of paramount interest due to its extensive use in numerous dynamic compression experiments. In this paper, we report nonequilibrium molecular dynamics simulation of shock compression in single-crystal Al to unfold structural PT at the atomic scale. Study along three major crystallographic orientations reveals that shock-induced fcc → hcp and fcc → bcc transitions are initiated at 18.8 and 30 GPa for the [001] direction and 32.2 (38) and 44 (46.1) GPa for the [110] ([111]) directions, respectively. Interestingly, these transition pressures are significantly lower than the values reported in the static compression experiment of Akahama *et al.* [Phys. Rev. Lett. **96**, 045505 (2006)] and the ramp compression experiment of Polsin *et al.* [Phys. Rev. Lett. **119**, 175702 (2017)]. Signatures of PT are identified from radial distribution function and virtual x-ray diffraction patterns. Domains of different phases are manifested in the pressure-temperature diagram of the principal Hugoniot.

I. INTRODUCTION

The propagation of shock waves in crystalline solids is often accompanied by polymorphic phase transitions (PTs). The rapid formation of new crystalline structures is one of the most interesting problems in shock wave physics and has tremendous application in strength enhancement and obtaining metastable high-pressure phases. The dynamic nature of PTs with the coexistence of different lattice structures is a special feature of shock waves [1], e.g., conversion of about 65% of α-Ti into the ω phase due to shock propagation [2], and the formation of diamond from polycrystalline graphite [3].

Aluminum is one of the most useful materials for many high-energy density systems. It is used as a flyer in gas-gun [4], high-explosive [5], and laser-driven [6,7] dynamic compression experiments and is a potential candidate for radiative ablators [8] in inertial confinement fusion experiments. Al and its alloys find important applications as structural components of spacecraft, impact shields, and many other systems that suffer from the potential risk of hypervelocity impact-induced damage [9]. Consequently, it is prudent to develop detailed knowledge of its microstructural response and polymorphic phase transformation under dynamic loading at extremely high strain rates.

At ambient conditions, metallic Al is stable in face-centered-cubic (fcc) form. Early first-principles density functional theory (DFT) calculations predicted an fcc → hcp → bcc PT path in bulk Al with transition pressures around 200 and 400 GPa [10,11], while the inclusion of phonon effects modified them to 205 and 565 GPa [12]. More recent calculations have a clear consensus on PT pressures of 176 and 373–380 GPa [13,14].

The hcp phase was observed at 217 GPa in a room-temperature (RT) diamond-anvil cell (DAC)

experiment [15,16]. Confirmation of a transition to a bcc structure initiating at 320 GPa and persisting up to 370 GPa came from a recent experiment combining synchrotron x-ray diffraction (XRD) with DAC [17].

While DAC experiments in association with the *in situ* XRD technique have enabled the study of structural PT under static loading conditions, there remains a lack of quantitative data on dynamic compression-induced PT, primarily due to the limitations in experimental techniques to capture these extremely rapid phenomena. The continuum-level measurement, traditionally used for the investigation of shock compressed targets, has severe limitations in resolving microstructural changes. Although shock recovery experiments are often used to quantify the structure-property relationships of materials exposed to uniaxial compression [18], it is nevertheless quite challenging to probe the incipient plasticity originated PT with them, primarily due to the instantaneous nature of PT, which is completely/partially reversible on shock release and, most importantly, the constructed phase being interspersed with multiple types of lattice defects. Current state-of-the-art synchrotron radiation and ultrafast laser-based visualization techniques are most suitable for observing lattice PTs [19]. The utilization of this technique yielded a direct observation of α-ε crystallographic PT in shocked iron [20,21].

Although numerous dynamic compression experiments have been reported, a *free-surface velocity* (FSV) profile has never been able to indicate a PT in Al [22]. Very recently, a laser-driven ramp compression experiment with nanosecond *in situ* XRD reported the observation of fcc → hcp and hcp → bcc transitions at 216 and 321 GPa, respectively, with the bcc phase extending up to 475 GPa [23,24]. The PT sequence and transition pressures are in close agreement with the static calculation and RT-DAC experiment. Subsequently, a nonequilibrium molecular dynamics (NEMD) simulation supported the experimental observations [25].
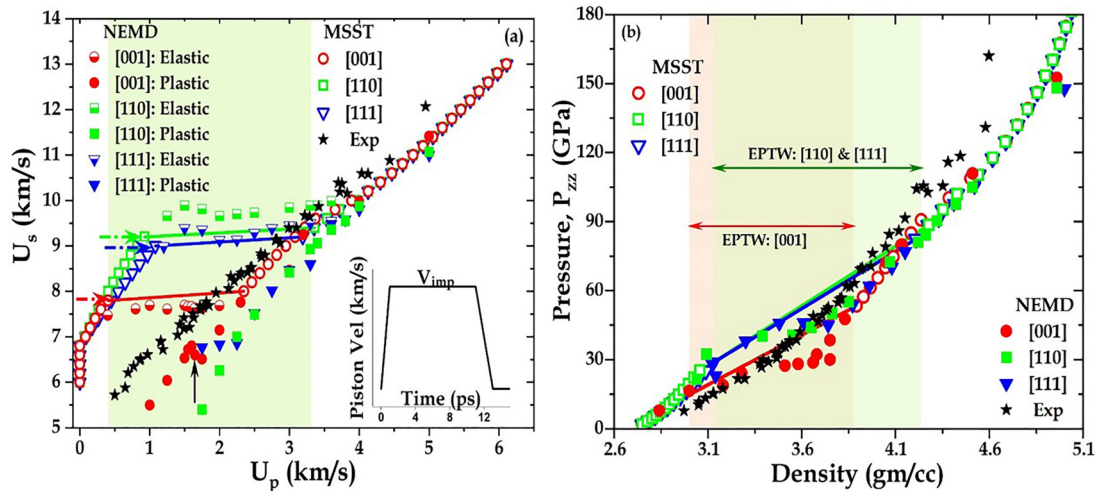
*basavaraj@barc.gov.in

FIG. 1. Shock Hugoniot of single-crystal Al along three different crystallographic directions: (a) Shock velocity vs particle velocity; (b) pressure (z component) vs density. The inset shows the time history of the piston velocity. In each case open circles represent MSST results, whereas half-solid and solid circles refer to NEMD data for the elastic and plastic waves, respectively. Experimental data are shown by stars.

The above discussion establishes that Al undergoes a solid-solid PT along both types of thermodynamic paths: RT isotherm (static loading) and isentropic compression. Hence, the obvious question is what happens to the lattice structure when Al is compressed along the principal Hugoniot (shock adiabat)? This paper attempts to answer this query from an atomistic perspective.

Phase boundaries in rapidly compressed solids strongly depend on the loading rate. In shock compression, material strength-dependent resistance causes the generation of significant shear stress. Since the shear relieving mechanism is either a structural phase transition or a plastic deformation, shock loading quite often leads to the lowering of transition pressures from hydrostatic values [26,27]. This motivates us to explore the shock-induced PT in single-crystal (sc)-Al.

To gain insight on the dynamic evolution of the crystal structure of this simple metal we have carried out systematic NEMD simulations of impact-induced shock propagation. It is shown that both fcc → hcp and fcc → bcc transitions occur at significantly lower pressures than the static compression experiments of Refs. [15,16] as well as ramp compression experiments of Refs. [23,24].

NEMD simulations have made it possible to accurately predict the shock-induced solid-solid PTs in Ga, Fe, and Cu at the atomic level [27–30], which tally with experiments. In a recent work, we have estimated the Hugoniot elastic limit (HEL) of submicron-thick sc-Ta by NEMD simulation and extrapolated the results to reproduce the experimental HEL of mm-thick targets with excellent accuracy [31].

II. SIMULATION METHOD

NEMD simulations have been performed to investigate piston impact-driven shock propagation in sc-Al along three different crystal orientations, namely, [001], [110], and [111]. In investigating dynamic compression-induced PT in ultrathin samples one needs to pay attention to the elastic-plastic two-wave (EPTW) region. The piston velocity ($V_{imp} =$

0.4–5.0 km/s) is tuned so as to capture the EPTW coupled structure for the chosen crystal orientations. The piston-velocity pulse shape [32] is shown in the inset of Fig. 1(a). We have also carried out equilibrium MD simulations using the multiscale shock technique (MSST) [33] with the shock velocity (U_s) varying from 6 to 13 km/s. The large-scale molecular dynamics code LAMMPS [34] is utilized for this purpose while the input crystal structures are created using ATOMSK [35]. More details of these simulations are provided in the Supplemental Material [32]. The interaction between atoms is treated by the embedded atom model (EAM) potential, parametrized by Winey *et al.* [36] which has been successfully utilized to address the shock Hugoniot, melting, and plasticity of sc-Al [37–39].

III. RESULTS

A. Shock Hugoniot and EPTW regime

The shock velocity (U_s) versus particle velocity (U_p) Hugoniot for three crystal directions are displayed in Fig. 1(a). NEMD results convey that for weak shocks, $U_p \leqslant U_{p_1}$ ($U_{p_1} \approx$ 0.5, 1.2, and 1.2 km/s for [001], [110], and [111] directions), defect-free sc-Al responds elastically. For intermediate velocities, $U_{p_1} < U_p \leqslant U_{p_2}$ with $U_{p_2} \approx$ 2.3, 3.6, and 3.6 km/s, the shock wave splits into a leading elastic wave (half-solid symbols) and a slower-moving plastic wave (solid symbols), thereby creating an elastic-plastic two-wave (EPTW) structure. The difference between the elastic and plastic wave velocity within the EPTW zone can be clearly seen in Fig. 1(a). Microstructural changes, lattice deformation, and crystal defects are initiated in this region. For $U_p > U_{p_2}$, a pure plastic wave travels into the medium.

The widely used MSST simulation on the other hand cannot resolve the EPTW region, but it nevertheless provides a good idea about the EPTW zone boundaries [solid lines of Fig. 1(a) joining the pure elastic and pure plastic ends].

The HEL (lower end of the EPTW region) for [001], [110], and [111] directions as clearly visible in the pressure
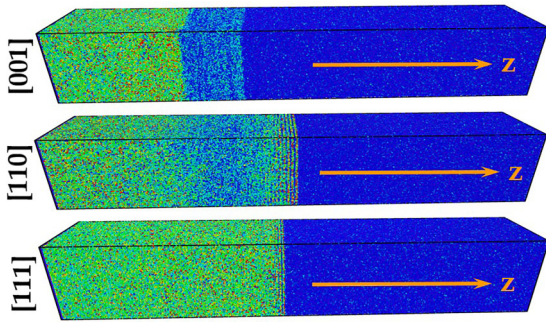
FIG. 2. Atomistic visualization of elastic-plastic wave propagation (along the z axis) after 6 ps due to impact at 1.5 km/s. Atoms are colored according to their kinetic energies with red being maximum and blue minimum (unshocked).

(P_H)-density (ρ) Hugoniot curves of Fig. 1(b) are 10, 25, and 28 GPa, respectively. In the case of uniaxial compression, it is appropriate to use the component of pressure along the shock direction, i.e., P_{zz} as the Hugoniot pressure. Our simulations thus reveal a strong crystal anisotropic effect in longitudinal stress at HEL. The plastic parts of the Hugoniot curves for three crystal orientations as obtained by both MSST and NEMD methods are indistinguishable and follow experimental data (stars) [40].

A distinct elastic-plastic feature is illustrated in the visualization plot of Fig. 2 displaying the kinetic energy distribution of atoms at 6 ps due to impact at 1.5 km/s. The clear appearance of a broad elastic zone and a well-separated plastic zone can be visualized for the [001] direction, whereas elastic precursors (fringes at the disturbance front), elastic dip, and the onset of a plastic wave can be observed for the [110] direction. The [111] direction exhibits feeble signatures of a two-wave structure at this time. This inherent anisotropy of the elastic properties as reported in Refs. [41,42] is also evidenced in the space-time evolution of longitudinal and transverse stresses (two representative impact cases are shown in Fig. S1 of the Supplemental Material [32]). Figures 1(a) and 2 also confirm that the compression-dependent longitudinal sound velocity is highest for the [110] and lowest for the [100] direction and for all three directions they agree with the experimental values [43].

The elastic-plastic transition can also be explained from the FSV profile of the sample, as presented in Fig. 3(a) ([001]) plotted for $V_{imp} = 1.5$ km/s. The arrows indicate the propagation of three different waves [44]. The three-wave feature would be less pronounced in a thicker sample due to the attenuation of the longitudinal stress associated with the elastic wave [45,46]. The FSV profiles for a wide range of impact velocities corresponding to three orientations are given
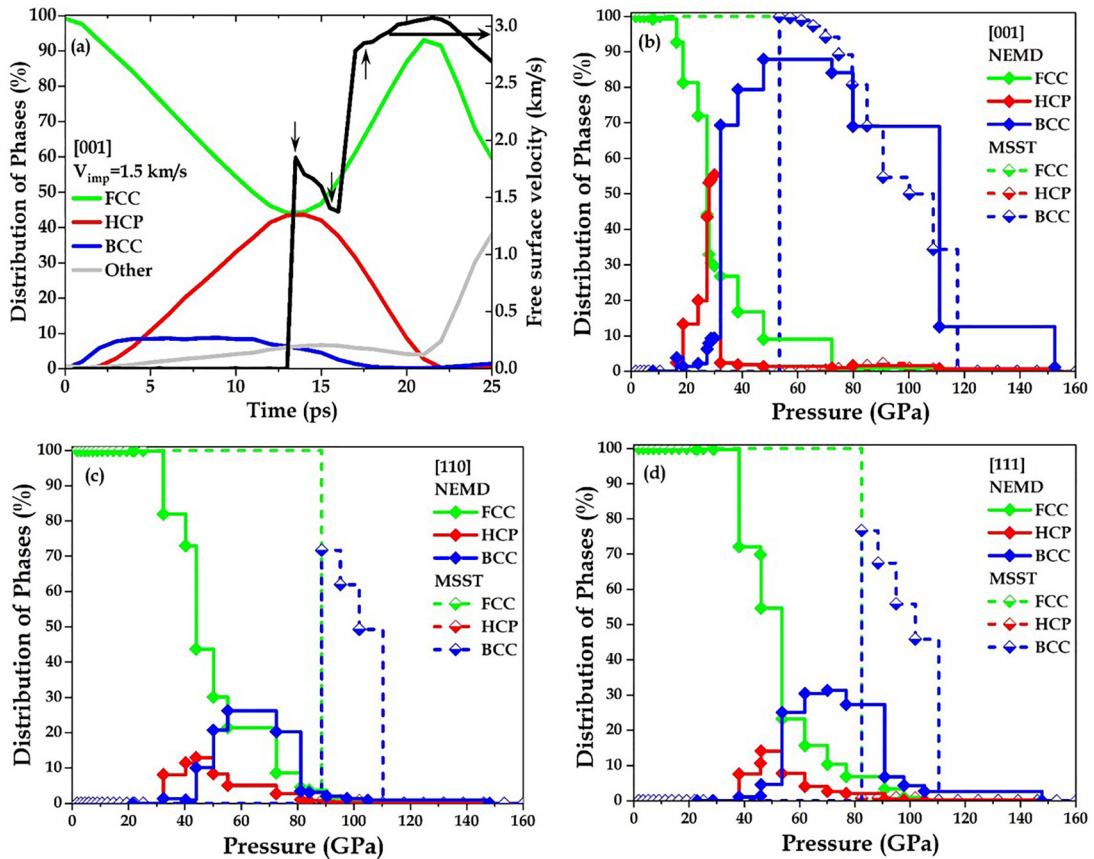

FIG. 3. (a) Time evolution of different structural phases (fcc, hcp, bcc, disordered) for [001] sc-Al due to impact at 1.5 km/s. The right axis shows the corresponding *free-surface velocity* profile. Statistics of different nucleated phases as a function of increasing pressure (P_{zz}) for shock traveling along the (b) [001], (c) [110], and (d) [111] directions. Results for NEMD (solid symbols–solid lines) and MSST (open symbols–dashed lines) simulations as obtained by iCNA are compared.

in Fig. S2 of the Supplemental Material [32]. Compression-rarefaction dynamics, showing the spatiotemporal evolution of P_{zz}, and the corresponding density and temperature within the 100-nm sample are presented in the contour plots in Figs. S3, S4, and S5 of the Supplemental Material [32].

B. Phase transition

To resolve local structural changes at the atomic level and extract information on the PT we have employed a heuristic crystal classification algorithm of the *interval common neighbor analysis* (iCNA) [47] as implemented in OVITO software [48]. To elucidate the dynamics of the PT we analyze the time evolution of different structural phases in [001] sc due to impact at 1.5 km/s as illustrated in Fig. 3(a). In the compression phase, the fcc atom fraction continuously decreases with time at the cost of increasing other regular structures (predominantly hcp) and becomes minimum when the elastic wave reaches the free surface (first arrow). It is interesting to observe that for this weak shock case, the crystal nearly reverts back to the original structure (an increase in the fcc count to 93% is an indication of recrystallization) on shock release. Thus, the PT in the elastic-plastic regime is reversible.

The percentage of atoms belonging to fcc (green), hcp (red), and bcc (blue) templates as generated for discrete values of V_{imp} along [001] sc are noted at the time when the fcc count is minimum. The resulting phase distribution as a function of increasing pressure (P_{zz}) is presented in Fig. 3(b). A similar exercise has been carried out for two other directions as well and the corresponding phase distributions are displayed in Figs. 3(c) ([110]) and 3(d) ([111]). For every pressure the remaining atoms belong to the noncrystalline structure [the gray line of Fig. 3(a) classified as "other"] arising due to various types of defects.

Thus, for a relatively soft material Al, a solid-solid PT along all three crystal directions is initiated even for weak plastic waves. It can be observed that with the increase in plastic pressure the fcc lattice initially transforms to the hcp and subsequently to the bcc phase. Although the sequence of the PT displayed in Figs. 3(b)–3(d) is analogous to static loading, nevertheless, a significant lowering in PT pressures is a special feature of shock loading. The conversions to both hcp and bcc phases depend on pressure in such a way that the number of atoms in the newly constructed phase relative to the original structure initially increases, reaches maximum, and finally reduces, paving the way for another phase, a crystal defect or melting as the case may be.

It can be noticed that shock-induced fcc $\rightarrow$ hcp and fcc $\rightarrow$ bcc transitions are triggered at 18.8 and 30 GPa, respectively, for the [001] direction, which are *one order magnitude less* than RT static compression and the 1000-K ramp compression values of Refs. [15,16,23]. The same for [110] sc are 32.2 and 44 GPa and for [111] sc are 38 and 46.1 GPa. Moreover, the [001] direction favors a phase change with a maximum of 55% hcp atoms occurring at 30 GPa and 88% of bcc atoms at 48 GPa. The corresponding maximum hcp conversions along the higher strength directions [110] and [111] are about 13% and 14% at 44 and 46 GPa, respectively. Similarly, the maximum bcc atom fractions along these directions are 26% and 31% with the transition pressure being 55 and 70 GPa.

Such anisotropy was also observed for another fcc metal, Cu [27]. Further, the bcc phase persists at maximum up to $\sim$110 GPa ([001]), which is significantly lower than the ramp compression pressure ($\sim$475 GPa).

The shock-induced PT has also been examined by MSST simulation and the resulting phase distributions are presented in Fig. 3 (half-solid symbols). The visualization of the atomic configuration with the iCNA predicted phase structures are portrayed in Fig. S6 of the Supplemental Material [32]. Noticeably, the equilibrium shock simulation shows only an fcc $\rightarrow$ bcc transition at the onset of the plastic Hugoniot (upper end of the EPTW regime) with pressures much higher than the corresponding NEMD case. Further, the phase fractions predicted by the MSST method deviate significantly from the NEMD case. The reason for this is that even though the MSST approach saves computational time while guaranteeing the simulation to reach the correct thermodynamic end state by controlling shock through prescribed continuum constraints, it does not predict crystal defects accurately.

C. Pressure-temperature phase diagram

Next, we analyze the role of shock heating on PT. The black line of Fig. 4 demonstrates the rise of shock temperature (T_H) of sc-Al along the principal Hugoniot. We have constructed pressure-temperature phase diagrams, i.e., domains of different phases achieved under uniaxial compression as displayed in the shaded regions. Considering every point on the black line as 100% atoms, the vertical line below passing through different color zones denotes the individual share of each template.

Even though it is difficult to capture signatures of PT from the P_H - ρ Hugoniot, the same is quite prominent in the P_H - T_H curve. Evidence of an appreciable conversion to hcp, bcc, and noncrystalline structures can be associated with a change in the slope of the curve at the arrow-marked pressures. Along with the strain rate-dependent plasticity and formation of defects with locally ordered structures, shock heating is also responsible for lowering the PT pressure. At low dynamic pressures, low heating facilitates compression of the fcc structure without PT, and a marginal increase in slope of the curve (between the first two arrows) indicates generation of stacking faults having local orders of the hcp structure. For still higher pressures, a steady rise of temperature initiates a bcc conversion. The plateau region (between the second and third arrow) for the [110] and [111] directions is originated from the dissipation of compression-generated mechanical energy through lattice deformation without generating any long-range ordered state. The third arrow specifies a rapid increase of disordered atoms making the sample approach a liquid state. This causes a significant difference in the phase diagram of the shock compressed sample from that of a hydrostatic one.

From the point of intersection of the P_H - T_H curve and the melting curve (static pressure versus melting temperature data) [49], we find that the shock-induced melting for the [001], [110], and [111] directions is initiated at 131, 138, and 135 GPa, respectively. The corresponding melting temperature for the [001] direction (4833 K) is consistent with other published work [14,37,50].
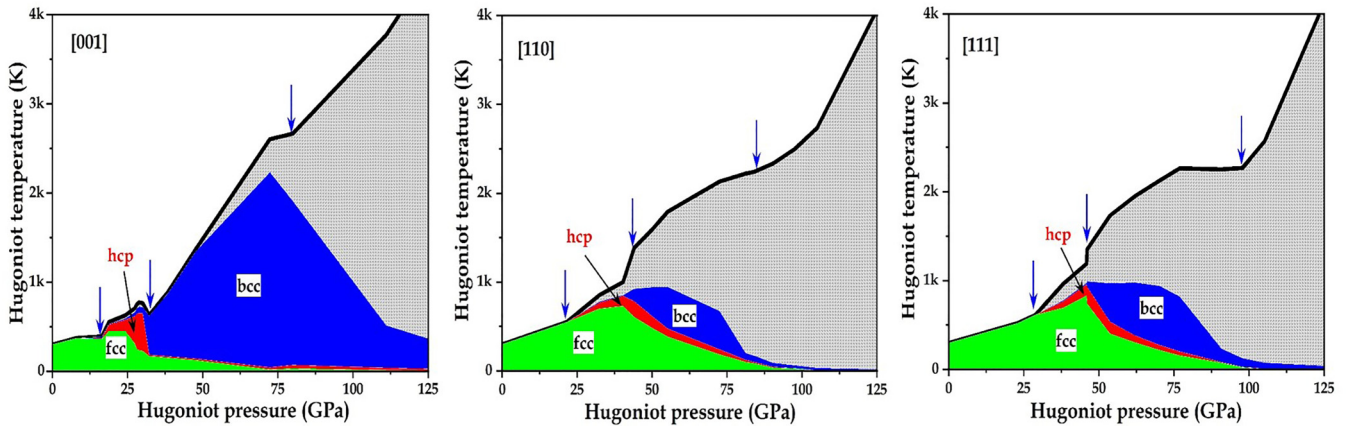
FIG. 4. Pressure-temperature phase diagram of uniaxially compressed sc-Al. The black solid line shows the rise of the shock temperature along the principal Hugoniot. The shaded area indicates P_H - T_H values for which pure fcc is observed and fcc-hcp, fcc-bcc, and fcc-hcp-bcc phases coexist.

D. Phase transformation dynamics

The phase transformation dynamics can be better appreciated from atomic configurations and sample radial distribution function (RDF) as displayed in Fig. 5 pertaining to two compressed states (6 and 10 ps) and two release states (18 and 22 ps) along the [001] direction. For 1.5 km/s, fcc → hcp is the predominant PT with its count initially increasing, reaching a maximum ($\sim$60%) at 14 ps, identified by the clear hcp peak in the RDF plot. The decrease of hcp atoms after shock unloading is associated with reverting back the crystal to the fcc structure as evidenced in the atomic configuration and RDF plots. A signature of recrystallization can be ascertained by noticing an almost similar profile of RDFs at 6 and 22 ps of Fig. 5, except for the presence of a few disordered atoms

FIG. 5. Left: Visualization of microstructure evolution along the [001] direction for V_{imp} = 1.5 km/s (top) and 3.0 km/s (bottom) at 6, 10, 14, 18, and 22 ps predicted by iCNA analysis. Green, red, and blue colors represent fcc, hcp, and bcc atoms, respectively, whereas gray refers to atoms of noncrystalline structures. Right: Corresponding radial distribution functions.

on shock release. Thus, it can be concluded that the incipient plasticity-induced PT is reversible. Incidentally reversible PT has been recently observed in plate impact experiments with the *in situ* XRD technique on the ionic crystal, CaF$_2$ [51].

A higher velocity impact (3.0 km/s) causes a significant rise in both shock pressure and temperature, leading to the collective movement of atoms, thereby adopting an open structure of bcc (valence electrons of compressed target commensurate interstitials of a bcc structure). The double-hump feature in the first peak visible in the RDF plot at 6 and 10 ps and at the shifted location for 14 ps of Fig. 5 is due to a bcc conversion. Visualization plots corroborate this. After shock breakout, the crystal exhibits a plastic deformation with a greater number of atoms losing long-range crystalline order as evidenced in the iCNA pattern and RDF profile at 18 ps. Fewer atoms still convert back to the original fcc phase. The occurrence of disorder atoms is further enhanced at 22 ps as reflected in the nearly flat RDF spectrum. Recrystallization to the fcc structure and reversibility of the PT on shock unloading have been observed for two other directions as well for low-impact strengths (refer to Fig. S7 of the Supplemental Material [32]), but the extent of reorientations is significantly less than that of the [001] direction. To sum up, it can be concluded that as the strength of the plastic wave increases, the PT switches from a reversible to an irreversible one. Shock-induced heating and energy dissipation due to plastic deformation is responsible for this. A further increase in shock strength causes a significant rise in the disorder atoms, eventually melting the solid in the compression phase itself.

Signatures of PT are also identified from virtual XRD (as implemented in LAMMPS) for three different impact velocities showing no PT, a maximum hcp phase, and a maximum bcc phase as shown in Fig. 6 (also shows the atomic configurations). The dynamic distributions of the phases for these velocities are presented in Fig. S8 of the Supplemental Material [32].

The planar fault analysis along with iCNA of the templates as depicted in Fig. S9 of the Supplemental Material [32] demonstrates that the hcp structures for all directions are locally ordered and they originate from stacking faults. The
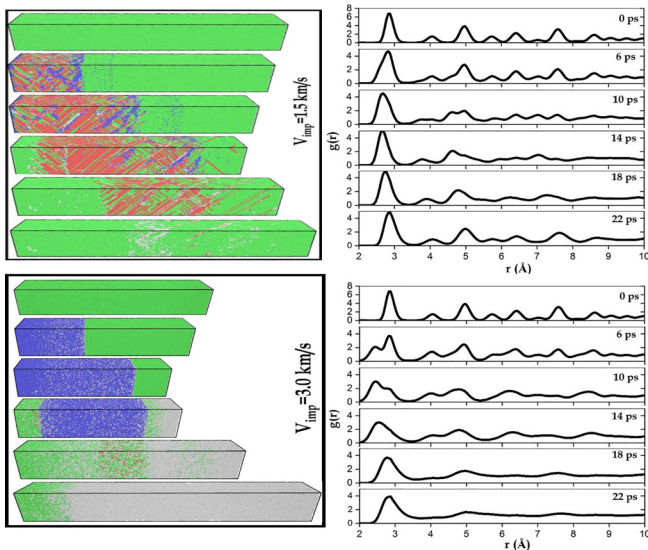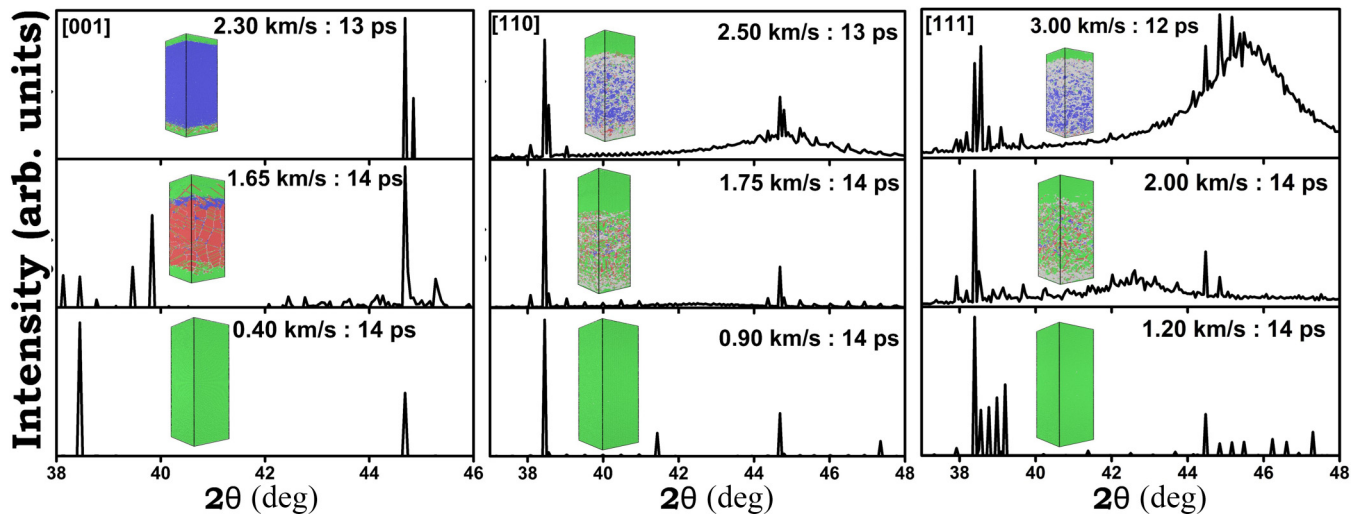
FIG. 6. Virtual XRD and visualization plots for three different impact cases with peaks showing a fcc structure (elastic wave), and maximum hcp and bcc phases. Color coding used for atoms is the same as in Fig. 5.

bcc structure generated in the [001] direction is a perfect crystal-phase transition with long-range order, however, in contrast, for the other two directions they are locally ordered with the presence of crystal defects. The generation of these locally ordered structures plays a key role in lowering the phase transition pressures in the shock compressed sample.

The incipient plasticity originated phase change is a transient feature with new phases partially/completely orienting back to the ambient structure on shock release. The interaction of a forward-moving compression wave and backward-moving rarefaction waves results in a reconstruction of the fcc structure to some extent, but largely destroys the structure, leading to an increasing number of disordered atoms. Newly constructed phases for both [110] and [111] single crystals are intertwined with defect atoms. This is precisely the reason why in spite of numerous shock wave experiments in Al, the continuum level measurement (FSV profile) did not reveal a shock-induced PT in Al.

IV. CONCLUSIONS

Nonequilibrium MD in conjunction with equilibrium MD (MSST) is employed to explore the shock-induced structural phase transition in single-crystal Al. The inevitable target heating and plastic deformation during uniaxial compression causes a huge disparity of PT pressures from that of static compression values. Our study also reveals that the structural phase transformation is strongly dependent on the shock propagation direction with respect to crystal orientation. Finally, we conclude that access to a dynamic compression experiment with *in situ* visualization techniques would offer a good platform to study shock-induced PT in Al.

ACKNOWLEDGMENT

[1] G. E. Duvall and R. A. Graham, Phase transitions under shock-wave loading, Rev. Mod. Phys. **49**, 523 (1977).

[2] D. R. Jones, B. M. Morrow, C. P. Trujillo, G. T. Gray III, and E. K. Cerreta, The α-ω phase transition in shock-loaded titanium, J. Appl. Phys. **122**, 045902 (2017).

[3] D. Kraus, A. Ravasio, M. Gauthier, D. O. Gericke, J. Vorberger, S. Frydrych, J. Helfrich, L. B. Fletcher, G. Schaumann, B. Nagler *et al.*, Nanosecond formation of diamond and lonsdaleite by shock compression of graphite, Nat. Commun. **7**, 10970 (2016).

[4] M. A. Zhaoxia, S. H. I. Anhua, L. I. Junling, L. I. U. Pei, and L. I. U. Sen, Radiation evolution characteristics of the ejecta cloud produced by aluminum projectiles hypervelocity impacting aluminum plates, Int. J. Impact Eng. **138**, 103480 (2020).

[5] D. C. Swift, C. A. Forest, D. A. Clark, W. T. Buttler, M. Marr-Lyon, and P. Rightley, On high explosive launching of

projectiles for shock physics experiments, Rev. Sci. Instrum. **78**, 063904 (2007).

[6] D. D. Mallick, M. Zhao, J. Parker, V. Kannan, B. T. Bosworth, D. Sagapuram, M. A. Foster, and K. T. Ramesh, Laser-driven flyers and nanosecond-resolved velocimetry for spall studies in thin metal foils, Exp. Mech. **59**, 611 (2019).

[7] L. Wang, Y. Yichao, W. Ji, W. Zhang, H. Jiang, W. Qin, Y. Wang, and D. Tang, Improving the energy conversion efficiency of a laser-driven flyer by an *in-situ* fabricated nano-absorption layer, Nanoscale Res. Lett. **15**, 125 (2020).

[8] D. C. Wilson, M. L. Spaeth, L. Yin, J. P. Sauppe, L. B. Hopkins, E. N. Loomis, R. F. Sacks, B. J. Albright, D. Strozzi, D. Munro *et al.*, Single and double shell ignition targets for the national ignition facility at 527 nm, Phys. Plasmas **28**, 052704 (2021).

[9] W. Song, Y. Lv, J. Li, C. Wang, and J. Ning, Influence of impact conditions on plasma generation during

hypervelocity impact by aluminum projectile, Phys. Plasmas **23**, 073506 (2016).

[10] P. K. Lam and M. L. Cohen, Calculation of high-pressure phases of Al, Phys. Rev. B **27**, 5986 (1983).

[11] F. Jona and P. M. Marcus, Lattice parameters of aluminium in the Mbar range by first-principles, J. Phys.: Condens. Matter **18**, 10881 (2006).

[12] J. C. Boettger and S. B. Trickey, High-precision calculation of the equation of state and crystallographic phase stability for aluminum, Phys. Rev. B **53**, 3007 (1996).

[13] M. J. Tambe, N. Bonini, and N. Marzari, Bulk aluminum at high pressure: A first-principles study, Phys. Rev. B **77**, 172102 (2008).

[14] T. Sjostrom, S. Crockett, and S. Rudin, Multiphase aluminum equations of state via density functional theory, Phys. Rev. B **94**, 144101 (2016).

[15] R. G. Greene, H. Luo, and A. L. Ruoff, Al as a simple solid: High pressure study to 220 GPa (2.2 Mbar), Phys. Rev. Lett. **73**, 2075 (1994).

[16] Y. Akahama, M. Nishimura, K. Kinoshita, H. Kawamura, and Y. Ohishi, Evidence of a fcc-hcp transition in aluminum at multimegabar pressure, Phys. Rev. Lett. **96**, 045505 (2006).

[17] G. Fiquet, C. Narayana, C. Bellin, A. Shukla, I. Esteve, A. L. Ruoff, G. Garbarino, and M. Mezouar, Structural phase transitions in aluminium above 320 GPa, C. R. Geosci. **351**, 243 (2019).

[18] H. Kishimura, S. Hamada, A. Aruga, and H. Matsumoto, Effect of shock compression on optical and structural properties of Eu_2O_3 and $Y_2O_3:Eu^{3+}$ powders, J. Appl. Phys. **119**, 205111 (2016).

[19] A. Higginbotham, P. G. Stubley, A. J. Comley, J. H. Eggert, J. M. Foster, D. H. Kalantar, D. McGonegle, S. Patel, L. J. Peacock, S. D. Rothman et al., Inelastic response of silicon to shock compression, Sci. Rep. **6**, 24211 (2016).

[20] D. H. Kalantar, J. F. Belak, G. W. Collins, J. D. Colvin, H. M. Davies, J. H. Eggert, T. C. Germann, J. Hawreliak, B. L. Holian, K. Kadau et al., Direct observation of the α-ε transition in shock-compressed iron via nanosecond x-ray diffraction, Phys. Rev. Lett. **95**, 075502 (2005).

[21] H. Hwang, E. Galtier, H. Cynn, I. Eom, S. H. Chun, Y. Bang, G. C. Hwang, J. Choi, T. Kim, M. Kong et al., Subnanosecond phase transition dynamics in laser-shocked iron, Sci. Adv. **6**, eaaz5132 (2020).

[22] W. J. Nellis, J. A. Moriarty, A. C. Mitchell, M. Ross, R. G. Dandrea, N. W. Ashcroft, N. C. Holmes, and G. R. Gathers, Metals physics at ultrahigh pressure: Aluminium, copper, and lead as prototypes, Phys. Rev. Lett. **60**, 1414 (1988).

[23] D. N. Polsin, D. E. Fratanduono, J. R. Rygg, A. Lazicki, R. F. Smith, J. H. Eggert, M. C. Gregor, B. H. Henderson, J. A. Delettrez, R. G. Kraus et al., Measurement of body-centered-cubic aluminum at 475 GPa, Phys. Rev. Lett. **119**, 175702 (2017).

[24] D. N. Polsin, D. E. Fratanduono, J. R. Rygg, A. Lazicki, R. F. Smith, J. H. Eggert, M. C. Gregor, B. J. Henderson, X. Gong, J. A. Delettrez et al., X-ray diffraction of ramp-compressed aluminum to 475 GPa, Phys. Plasma **25**, 082709 (2018).

[25] L. He, D. Polsin, S. Zhang, G. W. Collins, and N. Abdolrahim, Phase transformation path in zluminum under ramp compression; simulation and experimental study, Sci. Rep. **12**, 18954 (2022).

[26] E. E. McBride, A. Krygier, A. Ehnes, E. Galtier, M. Harmand, Z. Konôpková, H. J. Lee, H. P. Liermann, B. Nagler, A. Pelka et al., Phase transition lowering in dynamically compressed silicon, Nat. Phys. **15**, 89 (2019).

[27] A. Neogi and N. Mitra, A metastable phase of shocked bulk single crystal copper: An atomistic simulation study, Sci. Rep. **7**, 7337 (2017).

[28] K. Kadau, F. J. Cherne, R. Ravelo, and T. C. Germann, Shock-induced phase transformations in gallium single crystals by atomistic methods, Phys. Rev. B **88**, 144108 (2013).

[29] K. Kadau, T. C. Germann, P. S. Lomdahl, R. C. Albers, J. S. Wark, A. Higginbotham, and B. L. Holian, Shock waves in polycrystalline iron, Phys. Rev. Lett. **98**, 135701 (2007).

[30] K. Kadau, T. C. Germann, P. S. Lomdahl, and B. L. Holian, Atomistic simulations of shock-induced transformations and their orientation dependence in bcc Fe single crystals, Phys. Rev. B **72**, 064120 (2005).

[31] A. Singla and A. Ray, Hugoniot elastic limit of single-crystal tantalum at normal and elevated temperatures subjected to extreme strain rates, Phys. Rev. B **105**, 064102 (2022).

[32] See Supplemental Material at http://link.aps.org/supplemental/10.1103/PhysRevB.109.104101 for a description of the time history of the piston velocity.

[33] E. J. Reed, L. E. Fried, and J. D. Joannopoulus, A method for tractable dynamical studies of single and double shock compression, Phys. Rev. Lett. **90**, 235503 (2003).

[34] A. P. Thompson, H. M. Aktulga, R. Berger, D. S. Bolintineanu, W. M. Brown, P. S. Crozier, P. J. In't Veld, A. Kohlmeyer, S. G. Moore, T. D. Nguyen et al., LAMMPS - a flexible simulation tool for particle-based materials modeling at the atomic, meso, and continuum scales, Comput. Phys. Commun. **271**, 108171 (2022); https://www.lammps.org.

[35] P. Hirel, Atomsk: A tool for manipulating and converting atomic data files, Comput. Phys. Commun. **197**, 212 (2015); https://atomsk.univ-lille.fr.

[36] J. M. Winey, A. Kubota, and Y. M. Gupta, A thermodynamic approach to determine accurate potentials for molecular dynamics simulations: Thermoelastic response of aluminum, Modell. Simul. Mater. Sci. Eng. **17**, 055004 (2009).

[37] C. Pu, X. Yang, D. Xiao, and J. Cheng, Molecular dynamics simulations of shock melting in single crystal Al and Cu along the principle Hugoniot, Mater. Today Commun. **26**, 101990 (2021).

[38] X. Yang, X. Zeng, H. Chen, Y. Wang, L. He, and F. Wang, Molecular dynamics investigation on complete Mie-Grüneisen equation of state: Al and Pb as prototypes, J. Alloys Compd. **808**, 151702 (2019).

[39] S. Xue, Z. Fan, O. B. Lawal, R. Thevamaran, Q. Li, Y. Liu, K. Y. Yu, J. Wang, E. L. Thomas, H. Wang et al., High-velocity projectile impact induced 9R phase in ultrafine-grained aluminium, Nat. Commun. **8**, 1653 (2017).

[40] LASL Shock Hugoniot Data, edited by S. P. Marsh (University of California Press, Berkeley, CA, 1980), p. 165.

[41] J. A. Zimmerman, J. M. Winey, and Y. M. Gupta, Elastic anisotropy of shocked aluminum single crystals: Use of molecular dynamics simulations, Phys. Rev. B **83**, 184113 (2011).

[42] M. M. Budzevich, V. V. Zhakhovsky, C. T. White, and I. I. Oleynik, Evolution of shock-induced orientation-dependent

metastable states in crystalline aluminum, Phys. Rev. Lett. **109**, 125505 (2012).

[43] D. Choudhuri and Y. M. Gupta, Shock compression of aluminum single crystals to 70 GPa: Role of crystalline anisotropy, J. Appl. Phys. **114**, 153504 (2013).

[44] R. A. Austin, Elastic precursor wave decay in shock compressed aluminum over a wide range of temperature, J. Appl. Phys. **123**, 035103 (2018).

[45] R. Valisetty, A. Rajendran, G. Agarwal, A. Dongare, J. Ianni, and R. Namburu, HPC simulations of shock front evolution for a study of the shock precursor decay in a submicron thick nanocrystalline, Modell. Simul. Mater. Sci. Eng. **26**, 055008 (2018).

[46] B. Gurrutxaga-Lerma, D. S. Balint, D. Dini, D. E. Eakins, and A. P. Sutton, Attenuation of the dynamic yield point of shocked aluminum using elastodynamic simulations of dislocation dynamics, Phys. Rev. Lett. **114**, 174301 (2015).

[47] P. M. Larsen, Revisiting the common neighbour analysis and the centrosymmetry parameter, arXiv:2003.08879 (2020).

[48] A. Stukowski, Visualization and analysis of atomistic simulation data with OVITO - the open visualization tool, Modell. Simul. Mater. Sci. Eng. **18**, 015012 (2010); https://www.ovito.org.

[49] J. A. Moriarty, D. A. Young, and M. Ross, Theoretical study of the aluminum melting curve to very high pressure, Phys. Rev. B **30**, 578 (1984).

[50] L. He, F. Wang, X. Zeng, X. Yang, and Z. Qi, Atomic insights into shock-induced spallation of single-crystal aluminum through molecular dynamics modeling, Mech. Mater. **143**, 103343 (2020).

[51] P. Kalita, P. Specht, S. Root, N. Sinclair, A. Schuman, M. White, A. L. Cornelius, J. Smith, and S. Sinogeikin, Direct observations of a dynamically driven phase transition with *in situ* x-ray diffraction in a simple ionic crystal, Phys. Rev. Lett. **119**, 255701 (2017).